Journal of the European Ceramic Society **19** (1999) 1651–1664
© 1999 Elsevier Science Limited
Printed in Great Britain. All rights reserved
PII: S0955-2219(98)00261-1
0955-2219/99/$ - see front matter

Fabrication of Reaction-bonded Cr_2O_3 Ceramics

T. Li,* R. J. Brook and B. Derby

Department of Materials, University of Oxford, Oxford OX1 3PH, UK

(Received 14 July 1998; accepted 16 October 1998)

Abstract

Reaction-bonding to form Cr_2O_3 can be achieved by gaseous oxidation of a Cr phase. The reaction-bonding process is best conducted by complete oxidation before sintering. Below $\approx 800\,^{\circ}C$, the activation energy for oxidation is $220\,kJ\,mol^{-1}$, indicating the predominance of Cr^{3+} outward diffusion along high diffusivity paths, e.g., grain boundaries and dislocations. At higher temperatures, the activation energy is reduced to $52\,kJ\,mol^{-1}$ as a result of oxygen transport along lower-energy paths, e.g., along microcracks, and the internal and external surfaces. In spite of the decrease in activation energy, the access of oxygen to the inside of the powder compact is hindered by the progressive densification of the oxidizing powder compacts. Maximum densification is achieved for fully oxidized Cr/Cr_2O_3 compacts when the oxygen partial pressure is close to that of the $Cr\text{-}Cr_2O_3$ equilibrium. 0.1 wt% MgO addition increases the density and reduces the grain size of the reaction-bonded Cr_2O_3 samples due to the possible formation of the spinel phase $MgCr_2O_4$. ZrO_2 and MgO additions improve the fracture strength and toughness of conventionally sintered Cr_2O_3 and change its fracture mode from intergranular to intragranular. For reaction-bonded Cr_2O_3 samples with or without MgO addition, their fracture strength and toughness data are roughly the same as those of sintered Cr_2O_3 doped with ZrO_2 and MgO and their fracture surfaces are predominantly intragranular. © *1999 Elsevier Science Limited. All rights reserved*

Keywords: composites, sintering, transition metal oxides, Cr_2O_3, mechanical properties.

*To whom correspondence should be addressed at: Materials Research Center, Lehigh University, 5 E. Packer Avenue, Bethlehem, PA 18015, USA.

1 Introduction

Reaction-bonding process can be defined as a fabrication procedure in which the chemical reaction of the starting materials and the densification of the sample are both achieved in the same heating cycle. Depending on the material and process parameters, the two steps of reaction and densification can occur either in sequence or concurrently, or in some combination of these. Reaction-forming processes have been developed because they offer important advantages such as the near net-shape tailorability and glass-free grain boundaries. One of the major developments in reaction-forming has been reaction-bonded aluminum oxide (RBAO) starting from mechanically alloyed Al_2O_3/Al, $Al_2O_3/Al/ZrO_2$ or $Al_2O_3/Al/ZrO_2/Zr$ mixtures with low-to-zero shrinkage.[1,2]

Other material combinations are likely to be suitable candidates for this process, a number of metals exhibit a large volume expansion when oxidized. On the ground of (1) the volume expansion associated with oxidation of the metal and (2) the melting points of the metal and the resulting oxides, it is evident that the Cr/Cr_2O_3 system is a promising material combination for the study of the mechanism of consolidation during oxidation. Chromium has the following features: a large volume expansion on oxidation (102%) making it feasible to compensate compact shrinkage; a high melting point to ensure that a rigid shape is maintained during the whole process and to ensure that an interconnected pore structure is kept open throughout the oxidation. In the light of those advantages, reaction-bonded Cr_2O_3 was fabricated by oxidation of a Cr/Cr_2O_3 powder mixture in air at 1200 °C followed by densification of the as-oxidized powder compact in a controlled atmosphere at temperatures up to 1600 °C.[3,4]

With the aim of minimizing dimensional changes during the processing of powder preforms, a number of fabrication issues need to be more fully

understood. Those include oxidation of Cr in Cr/Cr_2O_3 powder preforms, densification of the as-oxidized Cr_2O_3 and the sequence of oxidation and densification. The oxidation of Cr is a strong exothermic reaction:

$$2Cr + 3/2O_2 = Cr_2O_3 \qquad \Delta H = -1139{\cdot}7\ kJ\ mol^{-1} \tag{1}$$

Cr_2O_3 is the only thermodynamically stable solid oxide in the Cr–O system at room temperature and atmospheric pressure. The oxidation of bulk Cr involves an initial logarithmic stage below $\approx$400 °C followed by a parabolic stage at higher temperatures.[5] Above $\approx$700 °C in air or oxygen, the reaction has generally been interpreted as parabolic, or as a sequence of parabolic stages resulting from repeated cracking of oxide scales apparently dependent on the pre-treatment of the metal and the reaction conditions.[6,7]

During oxidation, the dominant cation transport path in a polycrystalline oxide film is via the grain boundaries[8] and microstructural evidence[9] also supports this view. Barnes *et al.*[10] and Lees and Calvert[11] concluded that outward Cr transport is the only significant transport process at 850 °C (at least during the initial stage of oxidation); some inward oxygen transport occurred at 950 °C, probably along high diffusivity paths in addition to the outward Cr diffusion. The activation energy for Cr^{3+} outward diffusion along grain boundaries was measured as 250 kJ mol^{-1} (Ref. 12).

The fast diffusion paths may be grain boundaries[13] but may also be microcracks or pores.[14] The relative importance of chromium and oxygen diffusion is probably a function of the ambient oxygen pressure, the inward oxygen diffusion decreasing in importance with decreasing oxygen partial pressure.[6,15] The fact that the scales generally show a convex deformation suggests that oxide formation takes place in an outer section of the scale. Microcracks can develop in the growing oxide scale as a result of grain growth and fracture; they can then act as paths for rapid oxygen diffusion leading to an increased stress in the scale.[16]

Unlike the behaviour of bulk chromium samples, oxidation of chromium particles in a Cr/Cr_2O_3 powder compact is a new area of study, because the oxidation rate of chromium particles will depend not only on the activation energy of oxidation but also on the availability of oxygen inside a powder compact. The high melting points of both Cr and Cr_2O_3 mean that the oxidation of Cr in a Cr/Cr_2O_3 powder compact will involve solid phases, which is different from the RBAO process where the oxidation of Al proceeds by liquid/gas reactions above the melting point of Al. Furthermore, due to the large amount of heat released during oxidation, the heating cycle and atmosphere must be carefully chosen so that an interconnected pore structure is maintained to enable the complete oxidation of the Cr metal.

Despite apparent similarities with the RBAO process, there are a number of important differences. When Al oxidizes at low temperatures, it forms one of a complex series of metastable oxides depending on the oxidation conditions. As the temperature increases after oxidation, phase changes occur in the metastable oxide that can affect its mechanical integrity and also result in a fine grain size which aids subsequent sintering. With Cr oxidation on the other hand, as temperature increases at atmospheric pressure, volatile oxides form which inhibit densification. However, if oxidation of Cr to Cr_2O_3 is completed, sintering can then be carried out at low partial pressures of O_2, so that only one oxide phase is present throughout the reaction bonding process, making the Cr/Cr_2O_3 reaction bonding mechanism simpler than that operating during the formation of RBAO.

During densification, controlling the oxygen partial pressure is essential to obtain dense reaction-bonded Cr_2O_3 ceramic bodies. There is a substantial literature on the sintering of Cr_2O_3 (Refs 17–27); an overview has been given in Ref. 27.

The main objectives of this study were to (1) investigate the oxidation behavior of Cr in Cr/Cr_2O_3 powder preforms and the densification behavior of the as-oxidized Cr_2O_3 in the oxygen partial pressure generated by H_2/H_2O; (2) examine the microstructural evolution of samples undergoing this process in order to understand the mechanisms involved; and (3) characterize and compare the mechanical properties (flexural strength and toughness) of sintered Cr_2O_3 and reaction-bonded Cr_2O_3, correlating them with their microstructures.

2 Experimental Procedure

2.1 Starting materials

A 99·9% pure Cr powder (Aldrich Co.) with a medium particle size of 27·5 μm was used. Each single Cr particle consists of grains of $\approx$200 nm in size as revealed by transmission electron microscopy (TEM). The Cr_2O_3 powder used (Aldrich Co.) was 99·9% pure with an average particle size of 0·4 μm. 99·99% pure MgO (Aldrich Co.) with an average particle size of 0·3 μm was used as an additive.

2.2 Powder preform formation

The powders were wet ball-milled for 48 h in ethyl alcohol (> 99·7 vol%) with tetragonal-ZrO_2 balls

(⌀10 mm). The mass ratio of the milling media to the material was 10 to 1. During ball-milling, a small fraction of the Cr reacts with residual water to form amorphous hydrated oxides or hydroxides. There is also ZrO_2 introduced from the milling media. As a result, the as-prepared powder mixture is composed of Cr, Cr_2O_3, amorphous Cr_2O_3, ZrO_2 and other minor phases. The Cr content was determined by mixing 1 g of the powder in a dilute HCl solution forming a suspension. The Cr phase dissolves and the suspension is passed through a pre-weighed membrane filter of maximum pore size 0·2 μm. After drying the filter in an oven at 120 °C for 12 h, the weight of insoluble residual was measured and Cr content determined. The amount of ZrO_2 introduced during milling was determined by weighing the ZrO_2 milling media before and after ball milling. Two batches of powder were prepared with measured compositions (1) 42·3 vol% Cr, 52.5 vol% Cr_2O_3, 5.2 vol% ZrO_2 and (2) this same mixture but with 0·1 wt%MgO. The average particle size of Cr in the Cr/Cr_2O_3 powder mixture estimated from scanning electron microscopy (SEM) micrographs is reduced to around 10 μm and the Cr is homogeneously mixed with Cr_2O_3.

After ball-milling, the slurry was dried under an infrared lamp for 12 h. Next, the powder mixture was crushed with a mortar and pestle before being passed through a 65 μm sieve. The powders from different compositions were uniaxially pressed in hard steel dies using a hydraulic press to form green compacts of either cylindrical pellets (≈⌀11·0 mm×3·0 mm), or rectangular bars (≈26·0 mm×4·0 mm×2·5 mm). The pressure used was around 425 MPa, which yielded green compacts of moderate density [between 67 and 70% theoretical density (TD)].

2.3 Oxidation

Oxidation of the green pellets was conducted with a heating rate of 0·8 °C min^{-1} with the first hold at 1000 °C for 8 h and a second hold at 1200 °C for 15 h in air.

2.4 Densification

At the end of the oxidation stage, Ar (flow rate ≈30 ml min^{-1}) was used to purge the system before increasing the temperature further at a rate of 5 °C min^{-1}. A controlled H_2/H_2O gas mixture was introduced at 1400 °C at a rate of 20–40 ml min^{-1} to generate the appropriate oxygen partial pressure. Densification of the as-oxidized Cr_2O_3 was achieved up to 1600 °C in low oxygen partial pressures close to the Cr-Cr_2O_3 equilibrium. After a dwell at the sintering temperature of between 10 and 360 min, the furnace was cooled to room temperature under an argon atmosphere at a rate of 8 °C min^{-1}. Conventional sintering of Cr_2O_3 was conducted for mechanical property comparison. The processing conditions have been described by Li *et al.*[27]

2.5 Characterization

Median particle size, particle size distribution and the specific surface area of the powder mixtures were obtained by using a laser particle sizer (Malvern Instruments, Series 2600c). The densities of green and oxidized pellets were obtained by measuring their dimensions directly. Density and apparent porosity of sintered specimens were determined by Archimedes' method. The theoretical density for reaction-bonded samples was calculated as 5·25 g cm^{-3}. Thermogravimetry (TG) and differential thermal analysis (DTA) were conducted using a Netzsch Simultaneous Thermal Analysis System (STA 409) to characterize the oxidation mechanism of Cr in a Cr/Cr_2O_3 green compact when exposed to air. The dimensional changes of the powder preforms during reaction-bonding were measured continuously by a computerized pushrod dilatometer (Dilatronic IIRDP). To monitor the oxygen partial pressure continuously *in situ*, an oxygen sensor based on 5 wt% CaO stabilized ZrO_2 was connected to the exhaust of the worktube. The ratio of H_2/H_2O was regulated by adjusting the concentration of water vapor above the water or ice in a water bubbler. Oxygen partial pressures down to 10^{-30} atmosphere can be measured in a well-buffered system (e.g., H_2/H_2O, CO/CO_2).[28] Median pore radius of samples oxidized at different conditions was measured with a Micromeritics automated mercury porosimeter (AutoPore II 9240). In order to reveal the grain size and the distribution of secondary phases, polished specimens were thermally etched at 1200 °C for 30 min in air. Grain size in thermally etched specimens was determined using an image analyzer (KONTRON IBAS). X-ray diffraction (XRD) analysis (Philips 1310 with copper Kα radiation at 40 kV, 20 mA) was conducted to determine the phase evolution of samples during the reaction-bonding processes. Microstructure and element distribution were examined with transmission electron microscopy (TEM) (JEOL 200CX) and scanning electron microscopy (SEM) (PHILIPS 501) in secondary electron and backscattered modes, with energy dispersive X-ray spectroscopy (EDS) providing microanalysis.

2.6 Mechanical property test

A four-point bend test jig with a 10/20 mm span was used to evaluate the strength (modulus of rupture) of reaction-bonded Cr_2O_3 as well as of conventionally sintered Cr_2O_3. Specimens of

dimensions $\approx 27\,mm \times 4\,mm \times 2{\cdot}5\,mm$ were ground, and the tensile surface and the two sides of the bars were polished to dimensions $25\,mm \times 2{\cdot}5\,mm \times 2\,mm$ with a $1\,\mu m$ finish. The tests were conducted in an INSTRON machine (Model 1122) using a crosshead speed of $0{\cdot}5\,mm\,min^{-1}$. At least 10 samples were tested for each composition. The Vickers indentation technique was used to measure fracture toughness, K_{IC}, by measuring controlled crack lengths produced by a Vickers indentation machine (Vickers Armstrong Ltd, Series no. 23562) on polished surfaces of the specimens under a load of 5 kg. The relation of Anstis *et al.*[29] was used to calculate the fracture toughness and gives K_{IC} in units $MPa\,m^{1/2}$.

$$K_{IC} = 16 \times (E/H_v)^2 \times \left(P/c^{3/2}\right) \qquad (2)$$

where E is Young's modulus in GPa, H_v is the Vickers hardness in GPa, P is the applied load in N and c is the crack length in m. At least five indentations were performed for each estimation.

3 Results and Discussions

3.1 Determination of the reaction-bonding cycle

With the objective of near net-shape fabrication of Cr_2O_3 ceramics starting from Cr/Cr_2O_3 powder compacts, early attempts at overlapping oxidation of Cr in Ar containing O_2 impurities and sintering of as-oxidized Cr_2O_3 in H_2/H_2O at temperatures up to 1600 °C were made. This approach is based on the assumption that 'new' oxide will be sintered once it is formed. Furthermore, by controlling the relative rates of these steps, reaction-bonded Cr_2O_3 could be made with little dimensional change at any stage during processing. Experimental results revealed, however, that a considerable amount of the Cr metal phase remained in the sample and significant shrinkage (up to 30 vol%), due to sintering of the metal phase, occurred on subsequent heating. This can be attributed to the fact that the partial pressure of oxygen in argon ($\approx 10^{-6}$ atm) is not enough to oxidize the large fraction of Cr in the compact before the Cr particles become sintered together. Consequently, channels for oxygen transport are blocked. Cr ions have to travel through the oxide scales formed on the sintered Cr, which is a slow process and reduces the oxidation rate.

In view of the difficulties mentioned above and the very different oxygen pressures required for oxidation of Cr and sintering of Cr_2O_3, it is sensible to conclude that reaction-bonding Cr_2O_3 favors a cycle of oxidation before sintering. Thus, fabrication of reaction-bonded Cr_2O_3 ceramics consists of the following two separate stages:

- oxidation of the Cr pressed in Cr/Cr_2O_3 powder preforms, and
- sintering of the pre-existing and the as-oxidized Cr_2O_3.

3.2 Choice of oxidation conditions

Because of the large reaction exotherm, the heat evolved may result in local sintering of Cr, decreasing the surface area exposed to air and causing premature closure of oxygen transport paths. To achieve complete oxidation within a minimum period of time and at the lowest possible temperature so as to minimize grain growth, it is accordingly crucial to generate a structure allowing free access of oxygen. Ideally, a fully interconnected pore structure should be maintained during oxidation.

Oxidation of Cr in Cr/Cr_2O_3 was checked by XRD studies as well as by optical microscopic observation. Figure 1 displays a series of XRD spectra representing the phase evolution of Cr/Cr_2O_3 powder compacts containing 42·3 vol% Cr, oxidized under different conditions. Optical microscopy was employed to distinguish the metal phase from the oxide. XRD results show that only Cr_2O_3 peaks are present after 10 h at 1200 °C, while optical microscopic observation on a polished surface shows that the shiny Cr metal spots only disappear after a further 5 h. According to estimates made using the image analyzer, the amount of Cr phase after 2 h at 600 °C, 2 h at 1000 °C and 10 h at 1200 °C were about 82%, 44% and 1% of the amount of the Cr phase before oxidation, respectively. No ZrO_2 peak was detected by XRD.

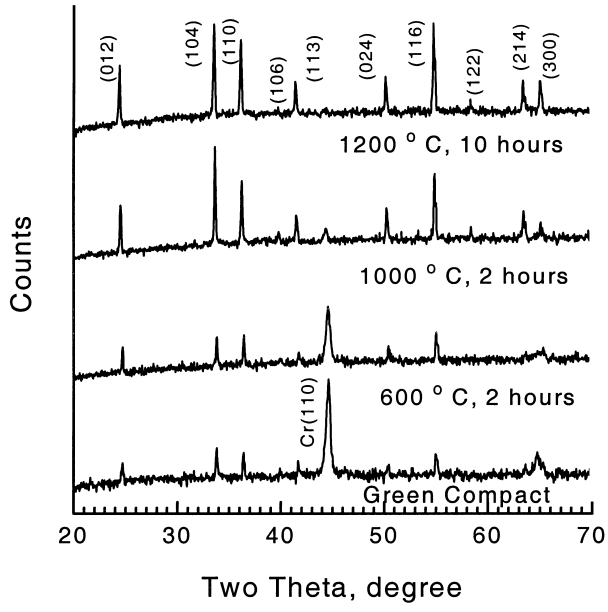

Fig. 1. Phase evolution during oxidation of Cr in Cr/Cr_2O_3 powder compacts. Peaks are from Cr_2O_3 except where labeled otherwise.

Weight loss of less than 0·1% was recorded after the as-oxidized samples were immersed in dilute HCl, which is assumed to dissolve all of the residual Cr metal phase. The as-oxidized samples exhibit a fully interconnected microstructure as shown in Fig. 2. The appearance of brighter areas around the continuous Cr_2O_3 phase is due to edge effects under the backscattered mode of SEM imaging.

3.3 Oxidation mechanisms

3.3.1 Thermal analysis

TG and DTA measurements of a green compact containing 42·3 vol% Cr were performed at temperatures up to 1200 °C and at a heating rate of 1 °C min^{-1} in air (Fig. 3). The TGA curve shows a small weight loss taking place around 200 °C at a slightly higher temperature than the sharp exothermic peak in the DTA curve. The sharp peak represents the large amount of heat released during the oxidation of residual alcohols from ball-milling. The weight loss also involves the decomposition of chromium hydroxide.

A considerable amount of volatile species are produced including H_2O, H_2, C_xH_y, CO, CO_2 and alcohols which were detected using the mass spectrometer. The evolution of these volatile species inside the powder compact takes time, which explains why the decomposition reaction appears first.

Above ≈290 °C, a weight gain is recorded, signifying the onset of Cr oxidation (Fig. 3). A strong broad exothermic peak is observed in the DTA curve across a wide temperature range up to 1200 °C. The sample increases weight rapidly and most of the Cr (over 98%) is oxidized over this temperature regime.

At atmospheric or near atmospheric oxygen pressures and at temperatures higher than ≈1000 °C, decomposition of Cr_2O_3 becomes important due to evaporation of CrO_3 via the following reversible reaction:[30–33]

$$Cr_2O_3 + 3/2O_2 = 2CrO_3 \qquad (3)$$

However, from the results, evaporation at higher temperatures does not affect the general behavior of the TG curve. Due to its volatile nature, the CrO_3 concentration could be monitored in the experiment. There was no significant variation with temperature.

TG analysis was also carried out under the actual oxidation conditions used with bulk specimens to understand the oxidation behavior at different temperatures and atmospheres. Figure 4 displays the variation of weight with the actual

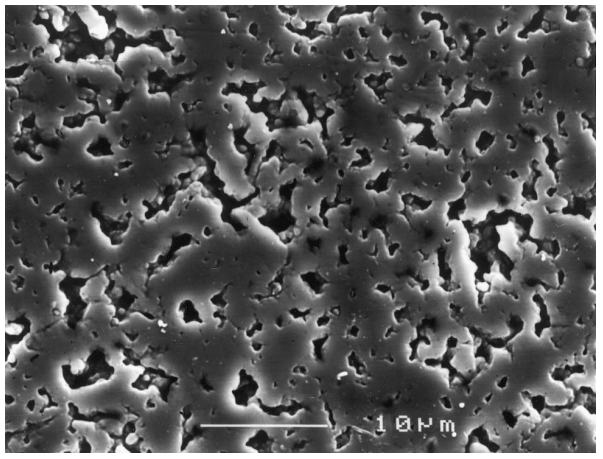

Fig. 2. SEM micrograph of polished surface of the as-oxidised Cr_2O_3 sample.

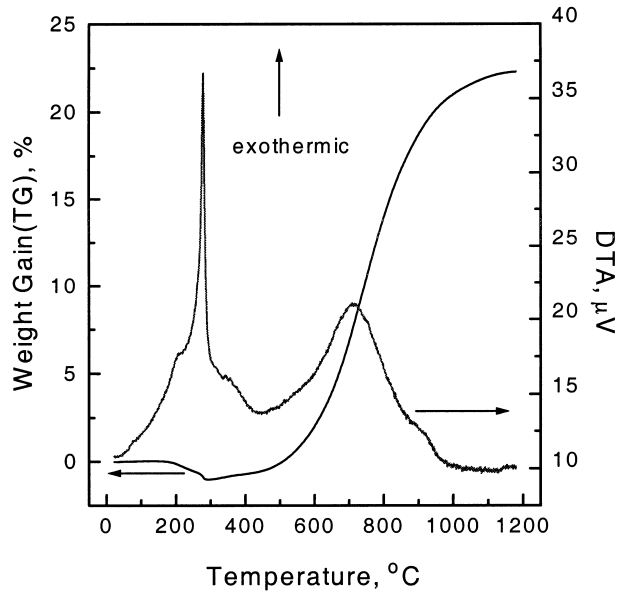

Fig. 3. TG and DTA analyses of the oxidation process of a Cr/Cr_2O_3 powder compact.

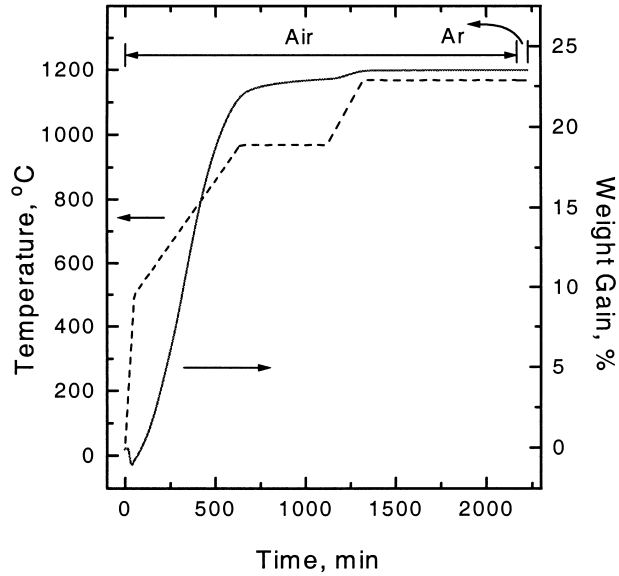

Fig. 4. TG analysis of the oxidation behavior of a Cr/Cr_2O_3 powder compact under the actual heating conditions. The solid line shows change in weight, the broken line shows the temperature profile.

heating cycle. No sudden weight increase occurred during the whole oxidation process, implying steady oxidation. The dimensional changes during oxidation were measured using a dilatometer. The results are depicted in Fig. 5. With an increase in temperature, the sample underwent a volume contraction of about 2% due to the evaporation of volatile species. Volume expansion does not begin until about 600 °C. When the sample had reached its former dimensions at about 800 °C, more than half of the Cr had been oxidized (Fig. 4). Further oxidation saw a net increase in volume of the sample. After complete oxidation, the Cr_2O_3 compacts had undergone a uniform volume expansion of $\approx$17% without cracking, and the density had increased from 67% to $\approx$80%TD. When Ar was introduced to purge the system, a volume expansion of about 0·4% was observed.

3.3.2 Activation energy of oxidation

In order to extract the data for calculating the activation energy of oxidation of Cr pressed in a Cr/Cr_2O_3 powder compact, isothermal oxidation studies were carried out at several temperatures (700, 750, 800, 900, 1000, 1100 and 1200 °C) under otherwise identical conditions.

During the initial oxidation stage, oxygen is assumed to have free access to the interior of the powder compact; the internal and external surface areas of all the powder compacts are thus the same. Atkinson[8] has proposed that, for powder systems, a parabolic law may be applied to the initial stage of isothermal oxidation when the oxide film thickness is greater than $\approx 1\,\mu$m for temperatures above $\approx$500 °C and when volume change and spallation of the oxide skin are not significant. Under these conditions, up to 22% of the Cr was oxidized within 2 min and the oxide scale formed is generally adherent. Oxidation during this early stage normally followed a parabolic law as shown in Fig. 6. However, after the initial oxidation stage, the oxidation rate is reduced for temperatures higher than 900 °C, because the large amount of heat released on oxidation above this temperature results in local sintering of the metal phase, reducing the contact area with oxygen and blocking oxygen passages.

Based on isothermal oxidation studies from 700 °C to 1200 °C, a series of parabolic rate constants were derived. Figure 7 displays the change in parabolic rate constant K as a function of inverse temperature. Two activation energies are identified in this temperature range, which makes it possible to differentiate the oxidation mechanisms. Below $\approx$800 °C, the measured activation energy of 220 kJ mol^{-1}, as shown in Fig. 7, is in good agreement with that of 250 kJ mol^{-1} measured for Cr^{3+} outward diffusion along grain boundaries,[12] indicating that Cr^{3+} outward diffusion along high diffusivity paths (i.e., grain boundaries, dislocations, etc.) is dominant in this temperature regime. For temperatures higher than $\approx$800 °C, the activation energy of oxidation is reduced to 52 kJ mol^{-1}, which is significantly lower than that for oxygen diffusion along grain boundaries in polycrystalline Cr_2O_3 (100 kJ mol^{-1}).[34] This suggests that a series step involving lower-energy oxygen transport paths becomes controlling, e.g., along microcracks, internal and external surfaces, as oxygen access to the oxidising surfaces becomes more difficult as a result of the increased density.

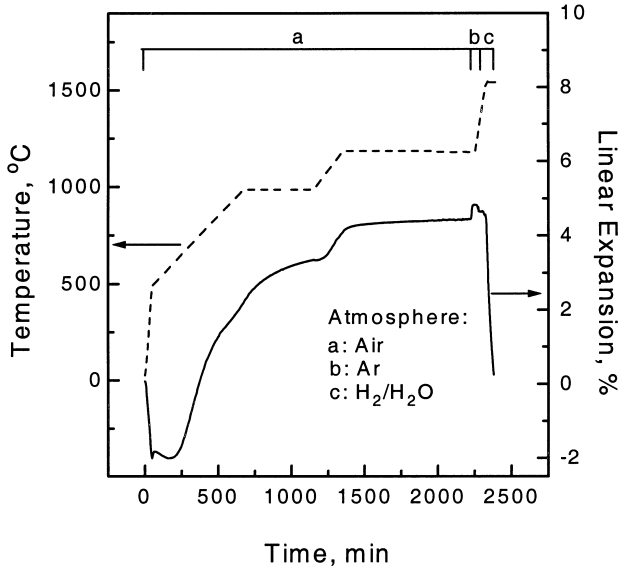

Fig. 5. Dilatometry measurement of the dimensional changes occuring during the reaction-bonding process. Sintering conditions: oxygen partial pressure: $3{\cdot}5\times10^{-13}$ atm; time: 1 h. The solid line shows the dimensional change of the sample. The broken line shows the temperature profile.

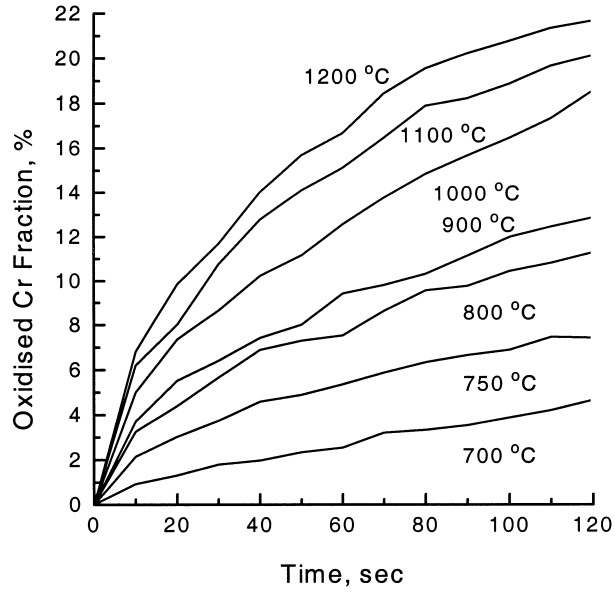

Fig. 6. Isothermal oxidation during the initial stage following a parabolic law.

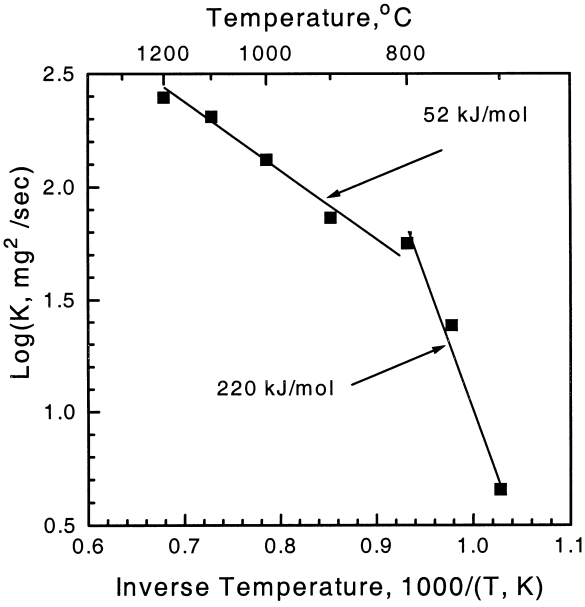

Fig. 7. Log K versus inverse temperature in isothermal oxidation of Cr/Cr_2O_3 powder preforms in air.

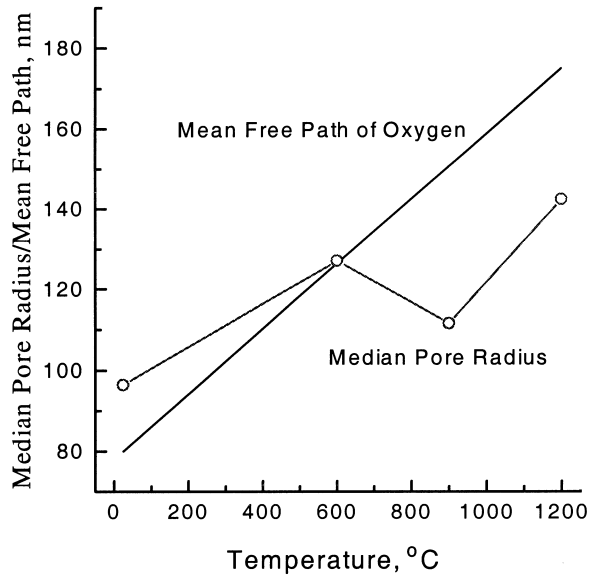

Fig. 8. The change of median pore radius of Cr/Cr_2O_3 powder compacts and mean free path of oxygen in air with temperature.

With an increase in temperature, a volume expansion of $\approx 17\%$ was observed for Cr/Cr_2O_3 powder compacts (Fig. 5), and the internal pore radius also increases. At the same time, the mean free path of oxygen increases and becomes increasingly larger than the pore radius. This phenomenon is demonstrated in Fig. 8 which shows the variation of the median pore radius and the mean free path of oxygen in air with temperature. The mean free path of oxygen in air as a function of temperature, quoted from Wu *et al.*,[1] is calculated according to the ideal gas equation and the Sutherland correction.

It has been proposed[35] that if the mean free path of a gas is larger than the pore radius, gas diffusion through a cylindrical pore system is hindered by the pore walls rather than by the interaction between gas molecules themselves. From Fig. 8, it can be seen that the value of the mean free path of oxygen becomes larger than that of the median pore radius at least at about 600 °C. This indicates that, above this temperature, the access of oxygen from ambient air is further restricted. Consequently, the diffusion of oxygen through the pore system is impeded and the rate of change of the constant K decreases with temperature above ≈ 800 °C (Fig. 7).

3.4 Microstructural development during oxidation

After wet ball-milling, Cr particles were covered with a thin film of Cr_2O_3 crystallites and sometimes amorphous chromium hydroxide as revealed by TEM. As the temperature began to increase, the reaction of the residual alcohols with oxygen and the decomposition of chromium hydroxide took place. The grain size of the eventual oxide film is found to be between 50 and 100 nm as shown in Fig. 9. No amorphous film was found above 300 °C.

The electrolytic chromium used has been found to contain microcracks, to have a grain size of about 200 nm, to possess inherent strain and to contain a large amount of oxygen and hydrogen.[36] To explain these effects, it has been proposed[37] that continuous or semi-continuous oxide membranes are formed on the grain surfaces of the metal during chromium electrolysis. The as-formed oxide membrane may be hydrated.[38] Upon heating, any water associated with the hydrated oxide will oxidize the surrounding metal and hydrogen will be given off in gaseous form by the reaction:

$$2Cr + 3H_2O = Cr_3O_3 + 3H_2(g) \qquad (4)$$

In order to reduce their surface energy, one of the consequences is that these oxide membranes at the surfaces of grains will spheroidize. This phenomenon

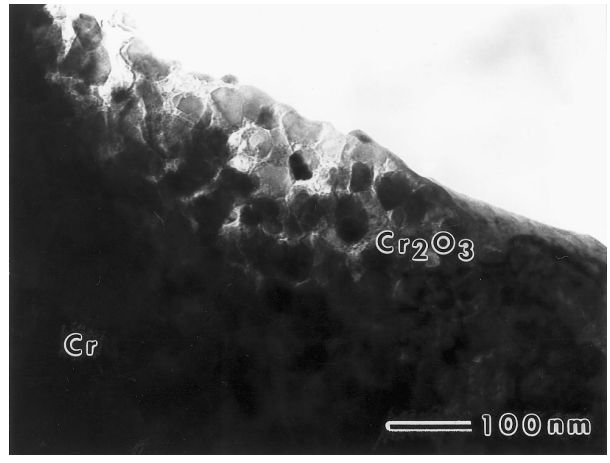

Fig. 9. Morphology of the oxide film after 30 min at 300 °C.

was observed in a sample oxidized at 500 °C for 30 min. The small dark particles of Cr_2O_3 are distributed uniformly on the surfaces of metal grains in a Cr particle as shown in Fig. 10. Coarsening of Cr grains and Cr_2O_3 particles was observed with rising temperature.

Figure 11 is a TEM micrograph of a sample oxidized at 800 °C for 30 min. Bigger Cr_2O_3 particles ($\approx$120 nm) were found decorating the grain boundaries of larger metal grains ($\approx$500 nm). The Cr grains grow because there is less constraint after the oxide membranes spheroidize into particles, and the oxide particles will coarsen at different rates because those on surfaces coarsen via surface diffusion and those on grain boundaries coarsen via grain boundary diffusion. Although coarsening of the Cr is inevitable after the spheroidization of the oxide membranes between grains, care must be taken to select a suitable heating cycle to promote grain growth and coalescence of Cr_2O_3 particles while suppressing Cr grain growth. Under such a heating cycle, Cr will be oxidized on a grain by grain basis rather than in a big particle or even in bulk form due to local Cr sintering. Thus, oxidation will occur in a minimum period of time.

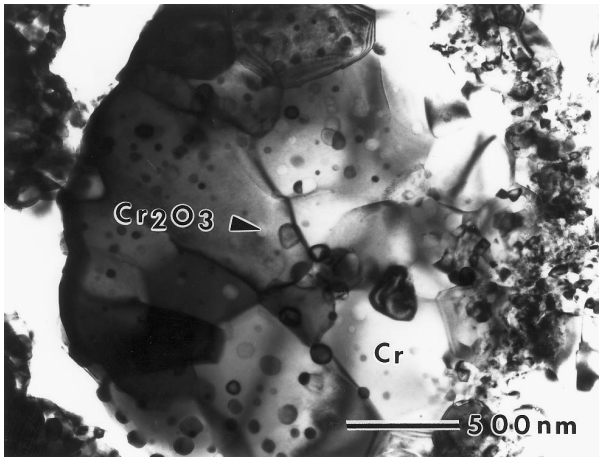

Fig. 10. Small Cr_2O_3 particles formed on the surfaces of Cr grains after 30 min at 500 °C.

With further oxidation, large stresses and strains developed in the oxide scale due to the 102% volume expansion during oxide growth and also from thermal mismatch because of the large difference in thermal expansion coefficients of Cr ($16{\cdot}2 \times 10^{-6}\,K^{-1}$ at 800 °C) and Cr_2O_3 ($7{\cdot}7 \times 10^{-6}\,K^{-1}$ at 800 °C). Spallation of the oxide scale occurred. Once the newly formed Cr_2O_3 is detached from the metal, it is impossible to distinguish the new oxide from the original oxide.

Above 1000 °C, evaporation of CrO_3 became prominent.[30–33] A considerable amount of grain growth of Cr_2O_3 and neck growth between Cr_2O_3 particles took place. Hench[21] proposed that the above phenomena at high oxygen partial pressures is due to surface diffusion and evaporation–condensation mechanisms because of the volatile CrO_3 species.

The 'new' and 'old' Cr_2O_3 have been partially bonded together as shown in a SEM image (Fig. 2) of a free surface of a fully oxidized sample. The grain size of the Cr_2O_3 is found to vary from a few tens of nanometers to a few microns. Figure 12 gives a detailed view of the structure of a Cr_2O_3 particle, showing the presence of well-developed fine Cr_2O_3 grains.

During oxidation of chromium, most of the second phase impurities are found to occupy free surfaces. ZrO_2 particles, which were introduced during ball-milling, are relatively coarse and have irregular shapes. Therefore, their effect as an oxygen active element during oxidation was limited.

3.5 Densification of fully oxidised Cr/Cr_2O_3 powder compacts

Oxygen partial pressure was found to be the most influential factor in controlling the densification of pure Cr_2O_3.[27] Sintering of Cr_2O_3 compacts oxidized

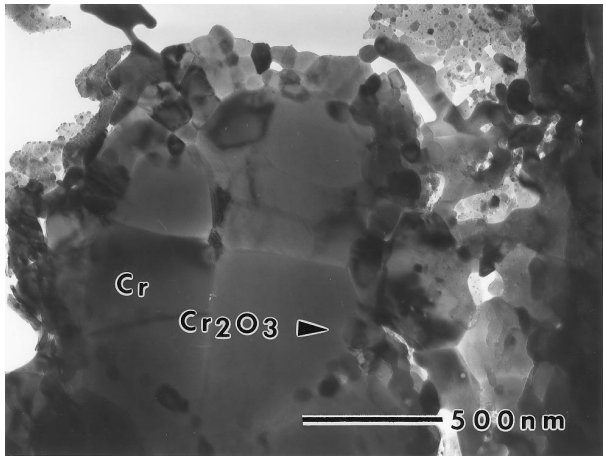

Fig. 11. Coarsening of the Cr and Cr_2O_3 particles at 800 °C for 30 min.

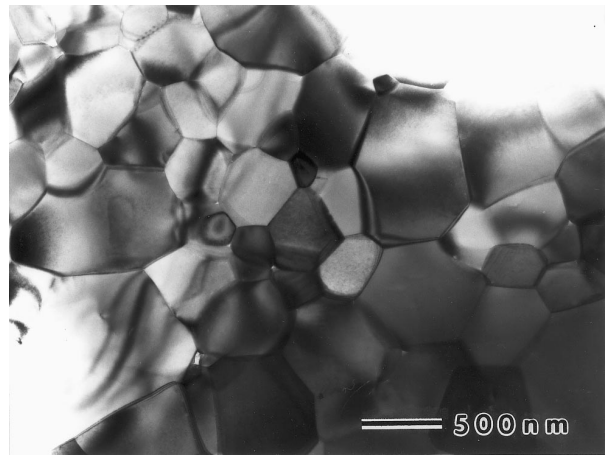

Fig. 12. TEM micrograph showing an equiaxed grain configuration of a fully oxidized sample.

from Cr/Cr_2O_3 powder preforms showed the same oxygen partial pressure dependence, as seen with pure Cr_2O_3 (Fig. 13). The sintered density reaches its maximum near Cr/Cr_2O_3 equilibrium conditions and densities of MgO doped samples are always higher than those of undoped samples over a wide span of pO_2. The probability of cracks occurring in doped samples was found to be less than that in undoped samples.

The dilatometry results in Fig. 5 show the dimensional changes taking place during the reaction-bonding of a Cr/Cr_2O_3 powder compact containing 42·3 vol% Cr. Upon completing oxidation and purging with Ar, introduction of a H_2/H_2O gas mixture initiates a dimensional shrinkage. Densification begins around 1500 °C. After reaching the sintering temperature of 1530 °C, rapid densification took place. Sintering for 1 h enabled the compact to achieve a density of 5·11 g cm^{-3} with a slight volume expansion above that of the starting green Cr/Cr_2O_3 compact.

The relationship between sintering time and density after reaction-bonding is shown in Fig. 14. It can be seen that, due to the rapid densification, a maximum density was achieved after about 60 min. Longer soaking time reduces the final density slightly, which is thought to be due to the loss of material through evaporation.

3.6 Microstructural development during densification

Figures 15 and 16 show the SEM micrographs of polished and thermally etched samples of reaction-bonded Cr_2O_3 and reaction-bonded Cr_2O_3 + 0·1 wt% MgO, respectively. It can be seen that considerable quantities of secondary phases occur mainly at grain boundaries. XRD results (Fig. 17) revealed that, apart from the tetragonal ZrO_2 phase, an unidentified phase also exists on the polished and thermally etched surface of a reaction-

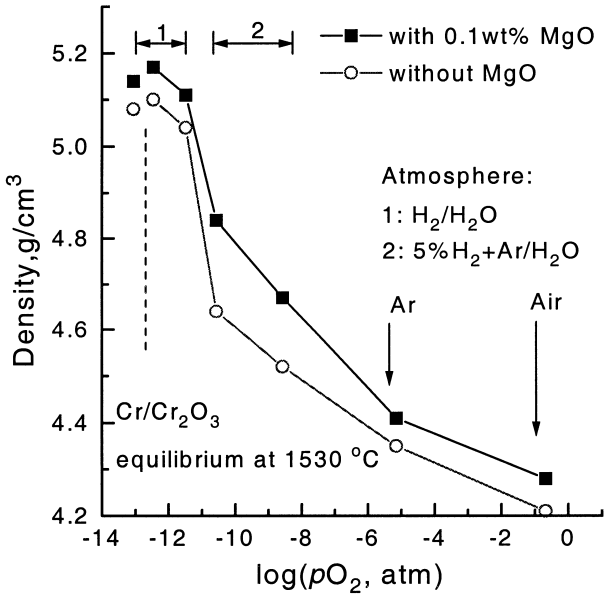

Fig. 13. Dependence of sintered density of oxidized Cr/Cr_2O_3 samples on oxygen partial pressure.

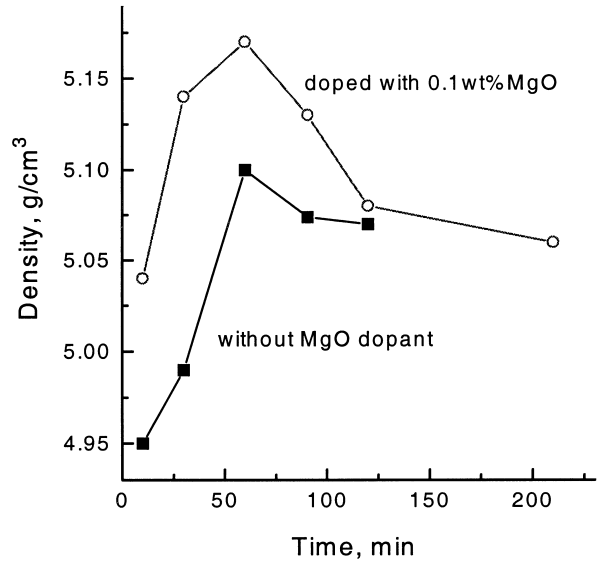

Fig. 14. Relationship between final density and soaking time at sintering temperature. Starting materials: 42·3 vol% Cr + 52·5 vol% Cr_2O_3 + 5·2 vol% ZrO_2.

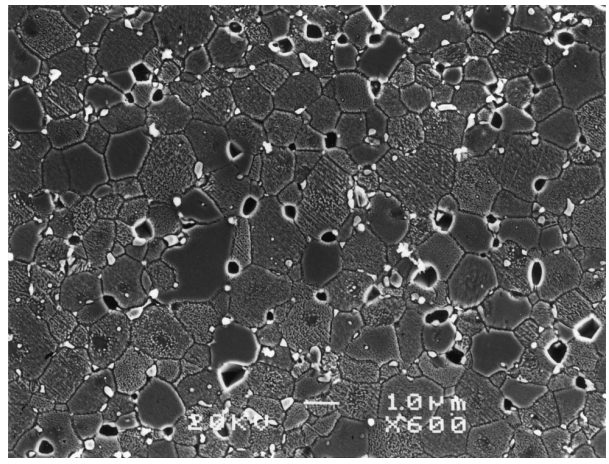

Fig. 15. SEM micrograph of a polished and thermally etched reaction-bonded Cr_2O_3 sample.

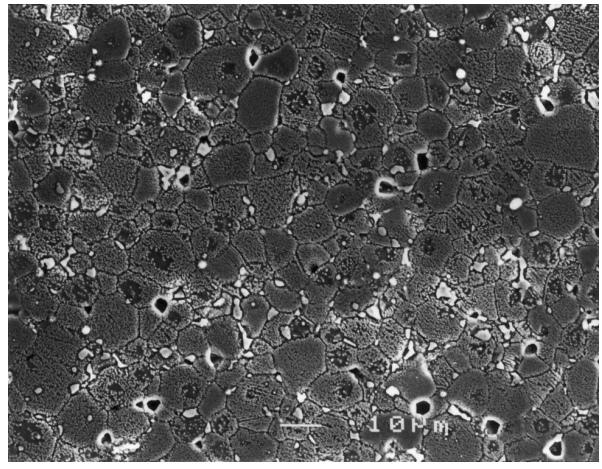

Fig. 16. SEM micrograph of a polished and thermally etched reaction-bonded Cr_2O_3 with 0·1 wt% MgO addition.

bonded $Cr_2O_3 + 0{\cdot}1$ wt% MgO sample. The strongest peak of this unknown phase is at the same position as a smaller unidentified peak in the $Cr_2O_3 + 1$ wt% $ZrO_2 + 0{\cdot}1$ wt% MgO sample.[27]

As the temperature rises from 1200 °C to the sintering temperature, grain growth takes place. The change in grain size with sintering time for the MgO doped and the undoped reaction-bonded Cr_2O_3 is illustrated in Fig. 18. The grain size of the doped Cr_2O_3 is consistently smaller than that of the undoped, suggesting grain growth is retarded by the addition of MgO possibly to form the spinel $MgCr_2O_4$.

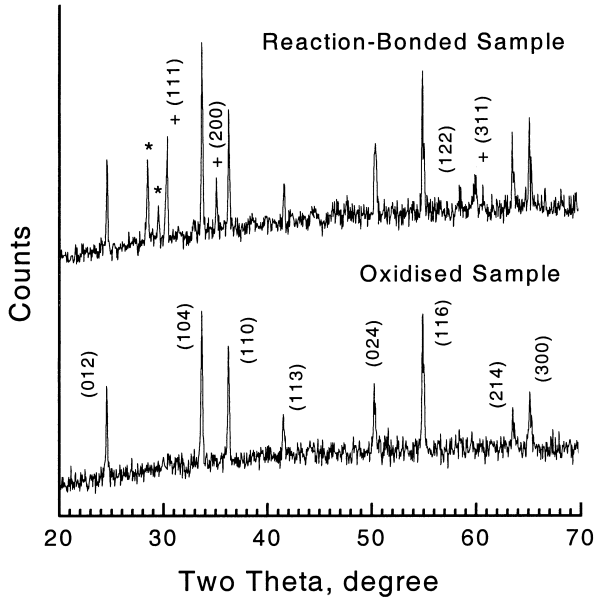

Fig. 17. XRD spectra from polished reaction-bonded and oxidized surfaces showing the phase development of the as-oxidized sample before and after sintering. *: an unidentified phase; +: t-ZrO_2; the indices are those of Cr_2O_3 unless otherwise stated. Starting powder: 42·3 vol% Cr + 52·5 vol% Cr_2O_3 + 5·2 vol% t-ZrO_2 + 0·1 wt% MgO.

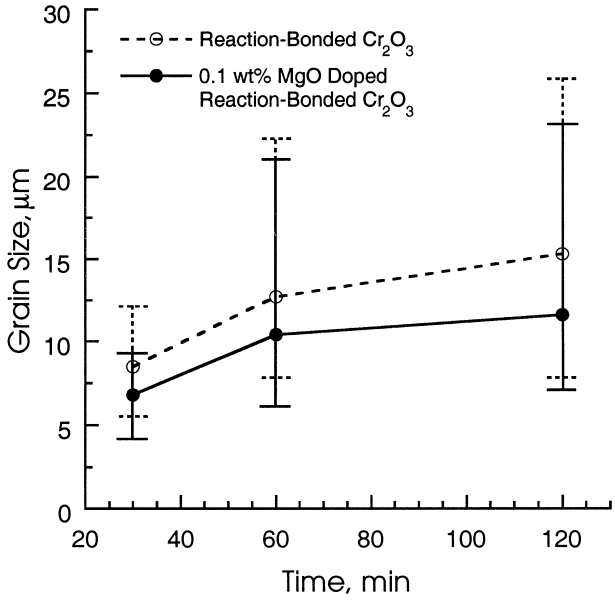

Fig. 18. Mean grain size of 0·1 wt% doped and undoped reaction-bonded Cr_2O_3 versus sintering time. Error bars indicate the maximum and minimum grain sizes measured.

3.7 Characterization of volume and density change in reaction-bonded Cr_2O_3

Since chromium doubles its volume upon oxidation, it is possible to predict the volume change of Cr/Cr_2O_3 during the reaction-bonding process, provided that the phase composition and density are known.

The theoretical relationship between the Cr solid volume fraction, V, and the green density of the pressed powder compact, D_G, at various values of porosity and volume shrinkage of fully reaction-bonded bodies can be expressed as follows:

$$V = \left(\frac{1-\rho}{D_G} - 1\right)/\chi \tag{5}$$

where ρ is the sum of porosity and volume shrinkage of the final product and χ is the volume expansion of Cr on oxidation, i.e., 102%. This relation can be applied to other metals if the corresponding parameters are used. From eqn (5), one can actually predict ρ, provided the solid volume fraction of metal and the relative green density are known. Figure 19 presents a series of curves that are the schematic representation of eqn (5).

Table 1 summarizes the data of volume and density after reaction-bonding a powder compact containing 42·3 vol% Cr with starting density 67·4% TD. According to Fig. 19, the predicted value (porosity + volume change) in the final product is 3·6% at the given Cr volume content and density of green pellet. This is in reasonably good

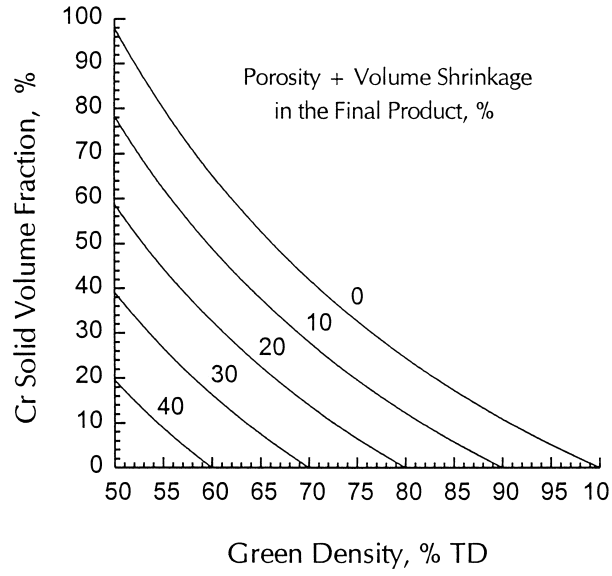

Fig. 19. Relationship between Cr solid volume fraction and the green density for various values of porosity + shrinkage in the final product.

Table 1. Volume and density data of a typical reaction-bonded Cr_2O_3 sample

Final density	*95·1% TD*
Linear shrinkage, radial	0·55%
Linear shrinkage, axial	−1·36%
Volume shrinkage	0·2%
Porosity	4·9%
Porosity + volume change	4·7%
Weight loss	1·4%

agreement with the measured value of 4·7%, if the effect of weight loss and the trace amount of impurities are taken into account.

3.8 Sintering mechanisms

Densification of the as-oxidized Cr_2O_3 powder compacts generally follows the same mechanisms proposed by Li *et al.*[27] for the densification of Cr_2O_3 + 1 wt% ZrO_2 + 0·1 wt% MgO. It has been found that, when sintered at 1530 °C under atmospheres with oxygen partial pressures close to the Cr-Cr_2O_3 equilibrium, addition of 1 wt% ZrO_2 and 0.1 wt% MgO increases the density of Cr_2O_3 to nearly full density in a shorter period of time. The rapid densification and higher final density are attributed to the appearance of a transient CrO liquid phase whose activity was lowered by the presence of ZrO_2 and MgO under low oxygen partial pressures and high temperatures.[27,39,40] Due to the existence of a significant amount of impurities such as ZrO_2, a transient CrO liquid phase forms at low oxygen partial pressures and high temperatures, promoting mass transport and enhancing densification. Reaction-bonding experiments also show that the addition of MgO reduces the number of cracks in the compacts after processing. This phenomenon may be related to the reduction of the overall dimensional change during oxidation. As revealed by X-ray mapping results, Mg segregates to grain boundaries. The MgO doped sample has a smaller grain size, suggesting that MgO has a retarding effect on grain growth possibly by forming a $MgCr2O_4$ spinel phase at the grain boundaries.[18,22,39]

To understand the effect of the oxidised Cr_2O_3 on the densification process, a method has been designed to establish the sinterability of the oxidised Cr_2O_3 particles in the Cr/Cr_2O_3 powder. A series of sintering experiments were conducted, using Cr_2O_3 + 5 wt% ZrO_2 powder compacts to simulate the original particles in the Cr/Cr_2O_3 powder, at 1530 °C for 1 h in low oxygen partial pressures ($3·2\times10^{-13}$ to $5·4\times10^{-13}$ atm) with different dwell times at 1200 °C. Figure 20 shows that the density decreases from ≈98%TD to ≈76%TD after 8·5 h dwell at 1200 °C, indicating the loss of driving force because of the time at the high temperature. However, the densification behaviour of fully oxidised Cr/Cr_2O_3 powder compacts has demonstrated that high densities have been achieved under the same conditions as used with the original Cr_2O_3 powder exposed in air at 1200 °C for 15 h. An apparent explanation is that the as-oxidized Cr_2O_3 mainly contributes to densification.

3.9 Mechanical property testing

3.9.1 Fracture strength and toughness

Experimental results have demonstrated that both sintered and reaction-bonded Cr_2O_3 exhibit radial-median cracks on indentation. Since minor cracks formed around the indent dissipate the crack energy, the K_{IC} value obtained is regarded as an upper bound. Table 2 shows the values of fracture

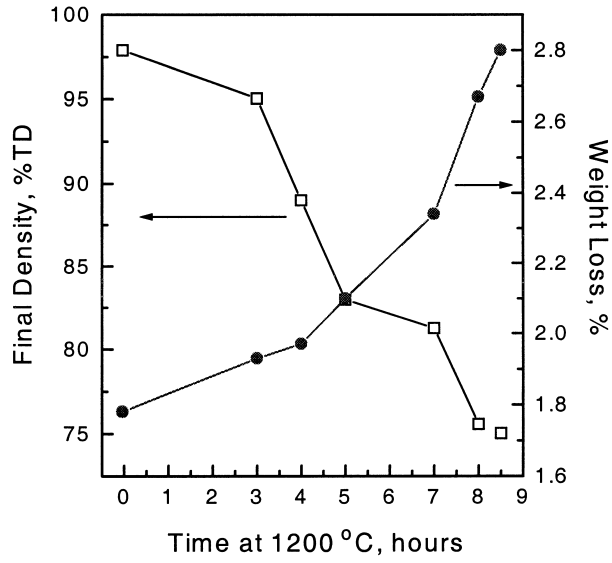

Fig. 20. Variation of the final density after sintering at 1530 °C for 1 h with different dwell times at 1200 °C. Starting powder: Cr_2O_3 + 5 wt% ZrO_2; green density: 65–66%TD.

Table 2. Fracture strength, toughness, porosity and mean grain size values of sintered and reaction-bonded Cr_2O_3

Materials	*Sintered Cr_2O_3*	*Sintered Cr_2O_3 + 1 wt% ZrO2 + 0·1 wt% MgO*	*Reaction-bonded Cr_2O_3*	*Reaction-bonded Cr_2O_3 + 0·1 wt% MgO*
K_{IC}, MPa m$^{1/2}$	3·23 ± 0·45	3·47 ± 0·32	3·73 ± 0.51	3·58 ± 0·47
Strength, MPa	178 ± 32	202 ± 27	220 ± 35	210 ± 42
Porosity, %	3·9 ± 0·4	1·8 ± 0·2	2·7 ± 0·3	1·2 ± 0·2
Grain Size, μm	9·2 ± 4·4	7·3 ± 2·6	8·5 ± 1·8	6·8 ± 2·2

strength, fracture toughness, porosity and mean grain size of sintered and fully reaction-bonded Cr_2O_3 held for 1 h at the sintering temperature. The mean grain sizes of these compositions are less than 10 μm.

For the sintered Cr_2O_3, the presence of ZrO_2 and MgO improved the fracture strength and toughness by a small amount, probably due to their enabling higher density, smaller grain size and a change of fracture mode from intergranular to intragranular. In spite of the relatively wide scatter of data, it can be noted that reaction-bonded materials exhibit higher fracture strength than sintered Cr_2O_3. On the other hand, because the mean and standard deviation of the strength and toughness data are roughly comparable, it is difficult to draw reliable conclusions regarding the differences in the mechanical behavior between the reaction-bonded Cr_2O_3 samples and the MgO-doped reaction-bonded Cr_2O_3 samples.

3.9.2 Fracture mode

Figures 21 and 22 are SEM micrographs illustrating the fracture modes of Cr_2O_3 and $Cr_2O_3 + 1$ wt% $ZrO_2 + 0.1$ wt% MgO, respectively. The fracture mode of Cr_2O_3 is mainly intergranular as expected. With the addition of ZrO_2 and MgO, the fracture mode changed to predominantly transgranular as seen by the presence of Cr_2O_3 grain cleavage facets. It is interesting to note that the change of fracture mode from intergranular to transgranular has also been observed in alumina on addition of nano-sized SiC particles.[41,42] Figures 23 and 24 show the fracture modes of reaction-bonded Cr_2O_3 with and without MgO addition, respectively. Reaction-bonded Cr_2O_3 exhibits a predominantly transgranular fracture mode, which corresponds to its higher strength and toughness. A similar fracture mode was observed for reaction-bonded Cr_2O_3 with 0.1 wt% MgO addition.

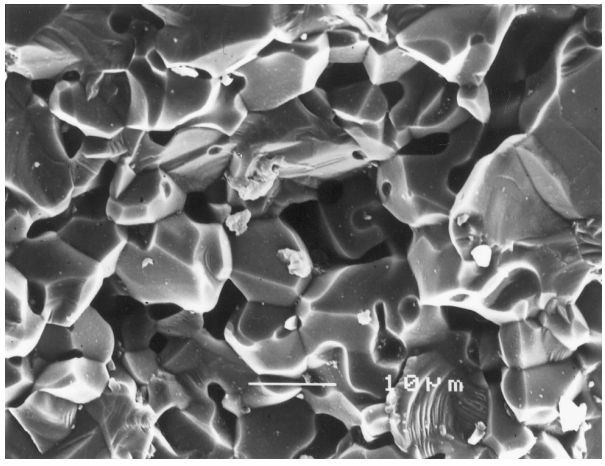

Fig. 21. SEM micrograph of a fracture surface of Cr_2O_3 showing an intergranular fracture mode.

Fig. 23. SEM micrograph of a fracture surface of reaction-bonded Cr_2O_3 showing a transgranular fracture mode.

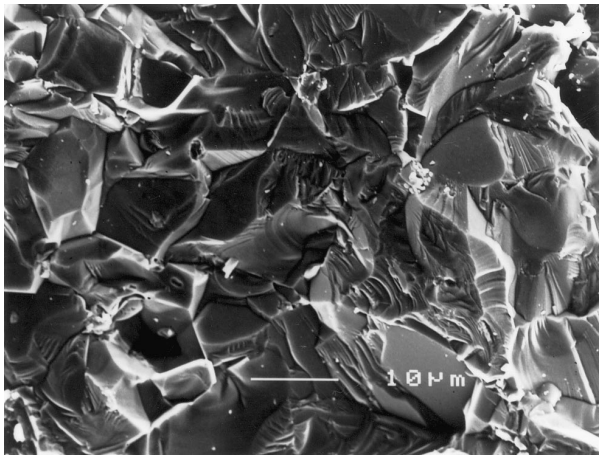

Fig. 22. SEM micrograph of a fracture surface of Cr_2O_3 + 1 wt% ZrO_2 + 1 wt% MgO exhibiting a predominantly transgranular fracture mode.

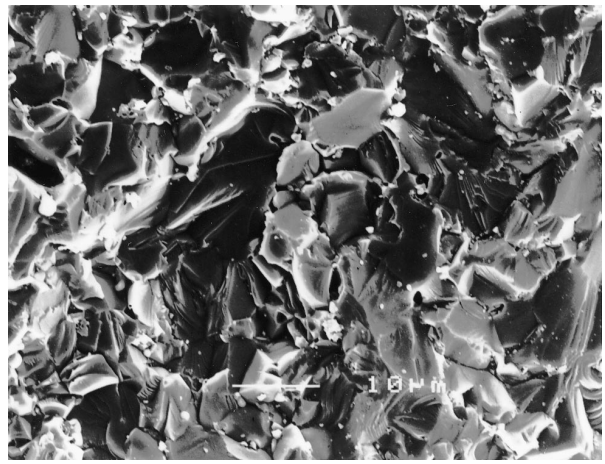

Fig. 24. SEM micrograph of a fracture surface of reaction-bonded $Cr_2O_3 + 0{\cdot}1$ wt% MgO showing a transgranular fracture mode.

4 Conclusions

1. The reaction-bonding of Cr_2O_3 best involves a cycle of complete oxidation before sintering. Being a strong exothermic reaction, the oxidation process must be carefully controlled to promote oxide formation around Cr grains, while suppressing Cr grain growth. In this way, Cr grains are oxidized individually and local sintering of the Cr phase is minimized. Consequently, complete oxidation is achieved in a minimum period of time and at the lowest temperature.
2. Below $\approx 800\,^{\circ}C$, the activation energy for oxidation is $220\,kJ\,mol^{-1}$, constitute with Cr^{3+} outward diffusion along high diffusivity paths (i.e., grain boundaries and dislocations). Consequently, new oxide formation takes place within the oxide scale or at the oxide/gas interface. At higher temperatures, the activation energy is reduced to $52\,kJ\,mol^{-1}$ as a result of interference by a new series mechanism involving transport along lower-energy paths, e.g., oxygen access along microcracks, and over the internal and external surfaces.
3. Maximum densification is achieved for the as-oxidized Cr_2O_3 compacts when the oxygen partial pressure is close to that of the Cr-Cr_2O_3 equilibrium. The Cr_2O_3 grains oxidized from Cr are sinterable and play a dominant role in the densification process. The MgO doped reaction-bonded Cr_2O_3 samples achieved higher density and had a smaller grain size than the reaction-bonded Cr_2O_3 sample, suggesting that MgO has a retarding effect on grain growth possibly by forming a $MgCr_2O_4$ spinel at grain boundaries.
4. For conventionally sintered Cr_2O_3 samples with average density of 96%TD, the fracture strength and fracture toughness are 178 MPa and $3.2\,MPa\,m^{1/2}$, respectively. The fracture surfaces exhibit a mainly intergranular fracture mode. When doped with 1 wt% ZrO_2 and 0.1 wt% MgO, Cr_2O_3 samples exhibit better mechanical properties, i.e., the fracture strength is 202 MPa and the fracture toughness $3.5\,MPa\,m^{1/2}$ because of the higher average density (98%TD), smaller grain size and change of fracture mode from intergranular to transgranular. The fracture strength and fracture toughness for the reaction-bonded Cr_2O_3 with an average density of 97%TD are 220 MPa and $3{\cdot}7\,MPa\,m^{1/2}$, respectively. 0·1 wt% MgO reaction-bonded Cr_2O_3 samples of an average density of 98%TD have a fracture strength of 210 MPa and a fracture toughness of $3{\cdot}6\,MPa\,m^{1/2}$. Both types of samples exhibit predominantly transgranular fracture.

References

1. Wu, S., Holz, D. and Claussen, N., Mechanisms and kinetics of reaction-bonded aluminum oxide ceramics. *J. Am. Ceram. Soc.*, 1993, **76**(4), 970–980.
2. Claussen, N., Wu, S. and Holz, D., Reaction-bonding of aluminum oxide (RBAO) composites: processing, reaction mechanisms and properties. *J. Eur. Ceram. Soc.*, 1994, **14**, 97–109.
3. Li, T., Brook, R. J. and Derby, B., Reaction-bonding of Cr_2O_3 ceramics. In *Ceramic Processing Science and Technology, 231–235, Proceedings of the International Conference on Ceramic Processing Science and Technology* Friedrishchafen, Germany, Sept. 1994.
4. Li, T., Brook, R. J. and Derby, B., Mechanisms of reaction-bonding of Cr_2O_3 ceramics. In *Fourth Euro Ceramics*, Vol. 2, ed. C. Galassi. Italy, Oct. 1995, pp. 157–162.
5. Young, D. J. and Cohen, M., Oxidation behaviour of chromium between 300 and 600 °C. *J. Electrochem. Soc.*, 1977, **124**, 769–774.
6. Lillerud, K. P. and Kofstad, P., On high temperature oxidation of chromium, I. Oxidation of annealed, thermally etched chromium at 800–1100 °C. *J. Electrochem. Soc.*, 1980, **127**, 2397–2410.
7. Kofstad, P. and Lillerud, K. P., On high temperature oxidation of chromium, II. Properties of Cr_2O_3 and the oxidation mechanism. *J. Electrochem. Soc.*, 1980, **127**, 2410–2419.
8. Atkinson, A., Transport processes during the growth of oxide films at elevated temperature. *Reviews of Modern Physics*, 1985, **57**, 437.
9. Polman, E. A., Fransen, T. and Gellings, P. J., The reactive element effect: ionic processes of grain-boundary segregation and diffusion in chromium oxide scales. *J. Phys.: Condens. Matter.*, 1989, **1**(28), 4497–4510.
10. Barnes, D. G., Calvert, J. M., Hay, K. A. and Lees, D. G., The role of oxygen transport in oxidation of Fe-Cr alloys. *Philos. Mag.*, 1973, **28**, 1303–1318.
11. Lees, D. G. and Calvert, J. M., The use of ^{18}O as a tracer to study the growth mechanisms of oxide scales. *Corrosion Science*, 1976, **16**, 767–774.
12. Hagel, W. C. and Seybolt, A. U., Cation diffusion in Cr_2O_3. *J. Electrochem. Soc.*, 1961, **108**, 1146–1152.
13. Rhines, F. N. and Wolf, J. S., The role of oxide microstructure and growth stresses in the high-temperature scaling of nickel. *Metallurgical Transaction*, 1970, **1**, 1701–1710.
14. Speight, M. V. and Harris, J. E., The generation of stresses in oxide films growing by cation diffusion. *Acta Metallurgica*, 1978, **26**, 1043–1045.
15. Lillerud, K. P. and Kofstad, P., Chromium transport through Cr_2O_3 scales: II. Changes in scale morphology during high vacuum treatment of oxidised chromium specimens. *Oxidation of Metals*, 1982, **17**, 195–203.
16. Kofstad, P., On the formation of porosity and microchannels in growing scales. *Oxidation of Metals*, 1985, **24**, 265–276.
17. Hagel, W. C., Jorgensen, P. J. and Tomalin, D. S., Initial sintering of α-Cr_2O_3. *J. Am. Ceram. Soc.*, 1966, **49**, 23–26.
18. Ownby, P. D. and Jungquist, G. E., Final sintering of Cr_2O_3. *J. Am. Ceram. Soc.*, 1972, **55**, 433–436.
19. Anderson, H. U., Influence of oxygen activity on the sintering of $MgCr_2O_4$. *J. Am. Ceram. Soc.*, 1974, **55**, 34–37.
20. Ownby, P. D., Oxidation state control of volatile species in sintering. In *Materials Science Research*, Vol. 6, ed. G. C. Kuczynski. Plenum Press, New York, 1973, pp. 431–437.

21. Hench, L. L., Sintering and reactions of magnesia and chromia. PhD thesis, Ohio State University, Columbus, 1964.
22. Roy, S. N., Saha, S. R. and Guha, S. K., Sintering kinetics of pure and doped chromium oxide. *J. Mater. Sci.*, 1986, **21**, 3673–3676.
23. Roy, S. N., Guha, S. K. and Maiti, H. S., Studies on the influence of lanthanum oxide on the sinterability of chromium(III) oxide. *J. Mater. Sci.*, 1990, **25**, 3508–3512.
24. Yamaguchi, A., Sintering of Cr_2O_3 in carbon powder. *Journal of the Ceramic Society of Japan*, 1980, **88**, 184–190.
25. Stone, H. E. N., Sintering in chromic oxide. *Metallurgia*, 1968, April 152–154.
26. Neve, J. M. and Coble, R. L., Initial sintering of Cr_2O_3. *J. Am. Ceram. Soc.*, 1974, **57**, 274–275.
27. Li, T., Brook, R. J. and Derby, B., Sintering of Cr_2O_3 in H_2/H_2O gas mixtures. *J. Eur. Ceram. Soc.*, 1999, **19**, 399–405.
28. Heyne, L., Some properties and applications of zirconia-based solid-electrolyte cells. In *Advances in Electrochemistry and Electrochemical Engineering*, Vol. 10, ed. H. Gerisher and T. W. Tobias. Wiley-Interscience, New York, 1977, pp. 65–88.
29. Anstis, G. R., Chantikul, P., Lawn, B. R. and Marshall, D. B., A critical evaluation of indentation techniques for measuring fracture toughness: I. Direct crack measurement. *J. Am. Ceram. Soc.*, 1981, **649**, 533–538.
30. Stearns, C. A., Kohl, F. J. and Fryburg, G. C., Oxidative vapourisation kinetics of Cr_2O_3 in oxygen from 1000–1300 °C. *J. Electrochem. Soc.*, 1974, **121**, 945–951.
31. Caplan, D. and Cohen, M., Volatilization of chromium oxide. *J. Electochem. Soc.*, 1961, **108**, 438–442.
32. Graham, H. C. and Davis, H. H., Oxidation/vapourization kinetics of Cr_2O_3. *J. Am. Ceram. Soc.*, 1971, **54**, 89–93.
33. Grimley, R. T., Burns, R. P. and Inghram, M. G., Thermodynamics of vapourization of Cr_2O_3. *J. Chem. Soc.*, 1961, **34**, 664–667.
34. Sockel, H. G., Saal, B. and Heilmaier, M., Determination of the grain boundary diffusion coefficient of oxygen in Cr_2O_3. *Surface and Interface Analysis*, 1988, **12**, 531–533.
35. Wutz, M., Adam, H. and Walcher, W., *Theorie und Praxis der Vakuumtechnik*. Friedrich Vieweg and Sohn, Braunschweig, Wiesbaden, Germany, 1988.
36. Sully, A. H. and Brandes, E. A., *Chromium*, 2nd ed. Butterworths, London, 1967.
37. Dennis, J. K. and Such, T. E., *Nickel and Chromium Plating*. Butterworths, London, 1986.
38. Gould, P. J., The oxidation of chromium and of chromium implanted with cerium. PhD thesis, University of London, London, 1992.
39. Ulmer, G. C. and White, W. B., Existence of chromium ion in the spinel solid solution series $FeCr_2O_4$–$MgCr_2O_4$. *J. Am. Ceram. Soc.*, 1966, **49**(1), 50–51.
40. Greskovich, C. and Stubican, V. S., Divalent chromium ion in magnesium-chromium spinels. *J. Phys. Chem. Solids*, 1966, **27**, 1379–1384.
41. Zhao, J., Stearns, L. C., Harmer, M. P., Chan, H. M., Miller, G. A. and Cook, R. C., Mechanical behaviour of Al_2O_3/SiC nanocomposites. *J. Am. Ceram. Soc.*, 1993, **76**, 503–510.
42. Borsa, C. E., Fabrication and mechanical properties of Al_2O_3/SiC nanocomposites. PhD thesis, University of Oxford, Oxford, UK, 1995.